ELSEVIER

Engineering Analysis with Boundary Elements **21** (1998) 117–129

Printed in Great Britain

PII: S0955-7997(97)00106-9

0955-7997/98/$19.00+0.00

A higher-order hypersingular boundary element method for the modeling of vortex sheet dynamics

Stéphan T. Grilli* & Zhimin Hu

Ocean Engineering Department, University of Rhode Island, Narragansett, Rhode Island, NY 02882, USA

A new model is proposed to compute the time evolution of interfaces between inviscid fluids represented by vortex sheets (VS), under the controlling effects of gravity, density difference, and interfacial tension. In this model, a higher-order boundary element method (BEM) is used to compute flow velocities on the VSs, based on Biot–Savart integral equations, and an explicit Taylor expansion scheme is used for time updating. An accurate numerical method is proposed to calculate hypersingular integrals occurring in the BEM.

Applications are presented for the steady flow around a circular cylinder, for the propagation of a nonlinear surface wave over constant depth, and for a periodic Kelvin–Helmholtz instability. The effects of model parameters on the accuracy of the solution are discussed. © 1998 Published by Elsevier Science Ltd. All rights reserved

Key words: Kelvin–Helmholtz instabilities, vortex sheet dynamics, Biot–Savart integral equations, boundary element method, interfacial waves.

1 INTRODUCTION

In the modeling of flows in stratified systems made of regions of ideal fluids separated by interfaces, vortex sheets (VSs) are used as an asymptotic model for the thin shear layers at the interfaces, in which the tangential velocity has a jump ΔV_s and vorticity has the local value, $\gamma = \Delta V_s$ (e.g., Batchelor,[1] Lamb[2]). In such systems, the VSs' strength $\gamma(t)$ changes with time due to both the density jumps and the surface tension effects at the interfaces. If no other vorticity is created inside the fluid regions and there is no external fluid flow, the flow results only from the VSs' effects; hence, when prescribing initial VS geometry and vorticity distributions, the flow calculation can be reduced to describing the time evolution of the VSs' geometry, kinematics, and strength.

In VS models of surface or interfacial waves, flow velocities are usually calculated using Biot–Savart (BS) integral equations (e.g., Batchelor[1]) and, typically, the VSs are discretized by a finite number of point vortices (e.g., Moore,[3] Rangel & Sirignano,[4] Zaroodny & Greenberg[5]), by piecewise-constant vortex distributions (PCVSs) (e.g., Fink & Soh,[6] Van de Vooren,[7] Grilli *et al.*[8]), or by higher-order methods (e.g., Baker *et al.*,[9] Hu & Grilli[10]). Point vortices have been shown to model well the initial deformation of interfacial waves but, after a large time, usually to exhibit non-physical chaotic motion;[3,11] the use of PCVSs and/or vortex regridding methods (introduced for instance by Rangel & Sirignano[4]) has been shown to reduce but not to totally eliminate such chaotic motion.

In fact, in stratified systems, as time increases, strong shear instabilities of the interfaces/VSs may develop, leading to VS roll-up[3,7] (this can, for instance, be seen in experiments with oil and water;[12] see also Fig. 1); such so-called Kelvin–Helmholtz (KH) instabilities intensify with an increase in ΔV_s, and decrease with an increase in density difference across the interface and/or interfacial tension[4] (see Grilli *et al.*[8] for a more detailed discussion of KH instabilities, particularly for the case of interfaces between oil and water). In point vortex representations, the singular terms in the BS integrals, representing vortex self-induced velocities, are neglected[6]; these terms, however, become large when, due to VS roll-up, the distance between vortices reduces, leading to increasing inaccuracies. In PCVS representations, the singular terms are calculated over each VS element as Cauchy principal

*To whom correspondence should be addressed. Email: grilli@mistral.oce.uri.edu

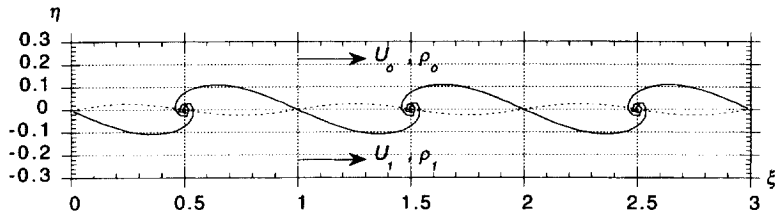

Fig. 1. Sketch of periodic Kelvin–Helmholtz instability with wavelength λ (with $\xi = x/\lambda, \eta = y/\lambda$) at the interface between two fluids. U_0, U_1 are uniform velocities and ρ_0, ρ_1 are densities of fluid 0 and 1, respectively. (- - - -): initial perturbation on the interface; (—): unstable interface computed at a later time (from Hu and Grilli[10]).

value integrals, with the approximation of constant local vorticity.[8] PCVS methods are thus more accurate but still give poor results when intense VS roll-up occurs, leading to close proximity of vortex elements and, hence, to inaccurate computation of BS integrals. Moore,[13] in fact, showed that a weak singularity does form on similarly discretized VSs, after a critical time beyond which numerical instability occurs. Meiron *et al.*[14] confirmed these findings and found a curvature singularity of the VSs. Krasny,[11] using discrete Fourier analysis, showed that numerical perturbations due to round-off errors in BS integrals are responsible for the observed irregular motion of point vortices.

The numerical instabilities observed in many VS computations are thus likely to be non-physical artifacts of both the selected method of discretization and the numerical integration of BS equations. To limit these instabilities, VS models should be able to correctly represent the intense VS roll-up that may occur during KH instability. This requires using a higher-order discretization of both the VSs' geometry and vorticity, together with an accurate integration of BS equations, including the correct representation of hypersingular terms. In this work, we have attempted to do so by developing and validating a higher-order VS BEM model. Cubic representations of both VS geometry and vorticity are introduced, based on the sliding polynomial method developed by Grilli & Subramanya.[15] An explicit time stepping method, based on a second-order Lagrangian Taylor series expansion, is used to calculate the VSs' time evolution. At each time step, discretized BS integrals are numerically integrated to calculate velocities along the VSs. The hypersingularities occurring in these integrals as a result of self-induced velocity terms are carefully analyzed using two methods: (i) a direct Taylor series expansion around the singular point; and (ii) a Laurent series expansion in the reference element containing the singular point.[16] Both methods are shown to provide identical results and allow us to accurately calculate the contributions of hypersingular terms in the BS integrals.

The VS models and the discretization/integration methods are validated using examples for the flow around a simple cylindrical geometry, and for the propagation of a nonlinear surface wave of permanent form over constant depth. An application of the model to the periodic KH instability of the interface between two fluids is finally presented (more results and details about this may be found in Hu & Grilli[10]).

2 THE MATHEMATICAL MODEL

2.1 Governing equations for flows induced by vortex sheets

In a two-dimensional stratified system in the vertical plane (x, y), made of incompressible, inviscid, irrotational fluid regions of constant density ρ, separated by interfaces modeled by VSs, the flow at any time t can be represented by a continuous velocity potential ϕ satisfying Laplace's equation. Due to the kinematic requirement of continuous normal velocity, the normal gradient of this potential is continuous through the interfaces $v_n = \partial\phi/\partial n$, but a jump in potential occurs at the interfaces/VSs between regions. The potential can thus be represented by a distribution of dipoles of strength δ (positive clockwise) along the VSs (Baker *et al.*[9])

$$\phi(x, y) = \int_{\Gamma(x')} \delta(s') \frac{\partial G}{\partial n}(\mathbf{x}, \mathbf{x}'(s'))\mathrm{d}s' \tag{1}$$

with $\mathbf{x} = (x, y)$ a point in the fluid regions, $\mathbf{x}' = (x'(s'), y'(s'))$ a point on the VSs represented by the closed (or infinite) boundary Γ, and s' the curvilinear abscissa along Γ; $G = (-1/2\pi)\log r$, with $r = \{(x-x')^2 + (y-y')^2\}^{1/2}$, is the free space Green's function, and $\mathbf{n}$ is the unit normal vector to an interface, pointing out of the region considered.

Introducing the complex notation $z = x + iy$, with $i = \sqrt{-1}$ and z^* the complex conjugate, we define the complex potential, $\Phi = \phi + i\psi$ (with ψ, the streamfunction) and the complex velocity, $q = u + iv$, with $q^* = \mathrm{d}\Phi/\mathrm{d}z$. Hence, eqn (1) can be transformed into

$$\Phi(z) = \frac{i}{2\pi} \int_{\Gamma(z')} \delta(z') \frac{\mathrm{d}z'}{z - z'} \tag{2}$$

with $z' = x'(s') + iy'(s')$. For a VS between two fluid regions, say Ω_0 and Ω_1 (e.g., Fig. 1), the dipole strength results from the potential jump at the interface; hence, $\delta(z') = \Phi_0 - \Phi_1 = \Delta\Phi$, and the potential on the VS is defined as $\Phi(z) = (\Phi_0 + \Phi_1)/2$, with the VS velocity being defined as, $q = (q_0 + q_1)/2$.

The VS's velocity can be expressed by differentiating eqn (2) with respect to $z \to \Gamma$ and integrating, as

$$q^*(z) = u - iv = \frac{dz}{dt} = \frac{i}{2\pi}\mathcal{P}\int_{\Gamma(z')}\gamma(s')\frac{ds'}{z - z'(s')} \tag{3}$$

with $\gamma = \partial\delta/\partial s = V_{0s} - V_{1s} = \Delta V_s$, the vortex sheet strength (i.e. vorticity), equal to the jump in tangential velocity V_s at the interface/VS; and d/dt, a Lagrangian time derivative operator, following the VS's motion. Eqn (3) is known as the Biot–Savart (BS) integral equation and, as point $z \in \Gamma$, it must be understood in a Cauchy principal value sense ($\mathcal{P}$).

In real form, eqn (3) reads

$$u(x, y) = \frac{dx}{dt} = \frac{1}{2\pi}\mathcal{P}\int_{\Gamma(s')}\frac{y - y'(s')}{r^2(s')}\gamma(s')ds' \tag{4}$$

$$v(x, y) = \frac{dy}{dt} = -\frac{1}{2\pi}\mathcal{P}\int_{\Gamma(s')}\frac{x - x'(s')}{r^2(s')}\gamma(s')ds'$$

For an infinite periodic interface between two fluids, with spatial periodicity λ (e.g. Fig. 1), eqn (3) transforms into

$$q^*(z) = \frac{i}{2\pi}\mathcal{P}\int_0^\lambda \gamma(s')\left\{\sum_{n=-\infty}^{+\infty}\frac{1}{z - z'(s') + m\lambda}\right\}ds' \tag{5}$$

with m an integral number. The summation formula (e.g., Van de Vooren[7])

$$\sum_{n=-\infty}^{+\infty}\frac{1}{z - z' + m\lambda} = \frac{\pi}{\lambda}\cot\frac{\pi}{\lambda}(z - z') \tag{6}$$

can be used and, hence,

$$q^*(z) = \frac{i}{2\lambda}\mathcal{P}\int_0^\lambda \gamma(s')\cot\frac{\pi}{\lambda}(z - z'(s'))ds' \tag{7}$$

which, in real form, reads

$$u(x, y) = \frac{dx}{dt} = \frac{1}{2\lambda}\mathcal{P}\int_0^\lambda \times \frac{\sinh\frac{2\pi}{\lambda}(y - y'(s'))}{\cosh\frac{2\pi}{\lambda}(y - y'(s')) - \cos\frac{2\pi}{\lambda}(x - x'(s'))}\gamma(s')ds'$$

$$v(x, y) = \frac{dy}{dt} = -\frac{1}{2\lambda}\mathcal{P}\int_0^\lambda \times \frac{\sin\frac{2\pi}{\lambda}(x - x'(s'))}{\cosh\frac{2\pi}{\lambda}(y - y'(s')) - \cos\frac{2\pi}{\lambda}(x - x'(s'))}\gamma(s')ds' \tag{8}$$

2.2 Time evolution of interfacial vorticity

Grilli *et al.*[8] derived the expression for the rate of change of VS strength γ as a function of time, due to gravity, density difference, surface tension effects at the interface between two ideal fluids of density ρ_0 and ρ_1, and interfacial tension σ_{01} (fluid 0 is above fluid 1; e.g. Fig. 1). This expression, which generalizes other similar expressions proposed by various researchers,[9,4,17,5] combines Euler equations for each fluid, on each side of the interface, with the pressure jump due to surface tension; it reads

$$\frac{d\gamma}{dt} = 2\kappa\left\{\frac{dV_s}{dt} + g\sin\beta + \frac{1}{4}\gamma\frac{\partial\gamma}{\partial s}\right\} - 2\frac{\sigma_{01}'}{1 + \varphi}\frac{\partial^2\beta}{\partial s^2} \tag{9}$$

with $\sigma_{01}' = \sigma_{01}/\rho_1$, $\varphi = \rho_0/\rho_1 \leq 1$, $\kappa = (1 - \varphi)/(1 + \varphi)$, the Atwood number, and $\partial\beta/\partial s$, the curvature. The tangential velocity at the interface is defined as $V_s = u\cos\beta + v\sin\beta$, with β the angle between the tangent to the interface and the x-axis; hence, the tangential acceleration reads

$$\frac{dV_s}{dt} = \frac{du}{dt}\cos\beta + \frac{dv}{dt}\sin\beta + \frac{d\beta}{dt}(v\cos\beta - u\sin\beta) \tag{10}$$

which can be further developed into

$$\frac{dV_s}{dt} = \frac{du}{dt}\cos\beta + \frac{dv}{dt}\sin\beta - \frac{1}{2}\frac{\partial\beta}{\partial s} \times \{(u^2 - v^2)\sin 2\beta - 2uv\cos 2\beta\} \tag{11}$$

in which

$$\cos\beta = \frac{\partial x}{\partial s} \text{ and } \sin\beta = \frac{\partial y}{\partial s} \tag{12}$$

have been used.

The VS accelerations, (du/dt, dv/dt), needed in eqn (11) may be obtained by Lagrangian time differentiation of BS eqn (3) for the non-periodic cases

$$\frac{dq^*}{dt}(z) = \frac{du}{dt} - i\frac{dv}{dt} = \frac{i}{2\pi}\mathcal{P}\int_{\Gamma(z')} \times \left\{\frac{d\gamma}{dt}(s')\frac{1}{z - z'(s')} - \gamma(s')\frac{q - q'(s')}{(z - z'(s'))^2}\right\}ds' \tag{13}$$

or BS eqn (7) for the periodic cases

$$\frac{dq^*}{dt}(z) = \frac{du}{dt} - i\frac{dv}{dt} = \frac{i}{2\lambda}\mathcal{P}\int_0^\lambda \times \left\{\frac{d\gamma}{dt}(s')\cot\frac{\pi}{\lambda}(z - z'(s')) + \frac{\pi}{\lambda}\gamma(s')\frac{q - q'(s')}{\sin^2\frac{\pi}{\lambda}(z - z'(s'))}\right\}ds' \tag{14}$$

3 THE NUMERICAL MODEL

3.1 Time marching

At any given time t, for a known distribution of VS strength/vorticity $\gamma(\mathbf{x}, t)$, the VS velocity ($u(\mathbf{x}, t)$, $v(\mathbf{x}, t)$), as well as the flow velocity anywhere else in the fluid regions, can be

explicitly calculated by discretizing and numerically integrating BS eqn (4) or eqn (8).

The same quantities can be calculated for a next time level, say $t+\Delta t$, by first time marching the VS geometry, through time integration of BS eqn (4) or eqn (8), to find $\mathbf{x}(t+\Delta t)$, then by time marching the VS strength, through time integration of eqns (9) and (11), to find $\gamma(\mathbf{x}, t+\Delta t)$.

In the present VS model, time marching is done using an explicit time stepping method based on truncated second-order Taylor series

$$\mathcal{F}(t+\Delta t)=\mathcal{F}(t)+\Delta t\frac{\mathrm{d}\mathcal{F}}{\mathrm{d}t}(t)+\frac{(\Delta t)^2}{2}\frac{\mathrm{d}^2\mathcal{F}}{\mathrm{d}t^2}(t)+O[(\Delta t)^3] \tag{15}$$

where $\mathcal{F}$ denotes any of x, y or γ, whose first-order time derivatives are given by eqn (4) or eqn (8), and eqns (9) and (11). Second-order time derivatives of $\mathbf{x}$, i.e. the accelerations, could be calculated by discretizing and integrating eqn (13) or eqn (14). As can be seen in these equations, however, $\mathrm{d}\gamma/\mathrm{d}t$ is included in the expressions of the VS accelerations, which makes eqn (9) (with eqn (11)) a Fredholm equation of the second kind for $\mathrm{d}\gamma/\mathrm{d}t$. This was pointed out by Baker *et al.*[9] who proposed an efficient iterative method for solving these equations. Rangel & Sirignano[4] mentioned a discretization and explicit solution of an algebraic system of equations to calculate the VS accelerations, and Grilli *et al.*[8] used a similar procedure in their piecewise-constant VS method. In the present study, since the focus is on the higher-order discretization and numerical treatments of hypersingular integrals, we decided, as was done in many earlier VS models, to simply calculate the VS accelerations used in eqns (11) and (15) by a backward finite time difference of velocities, involving several time levels. (Note that an Adams–Moulton predictor–corrector method could be used as well, as in Stansby & Slaouti.[17]) It is expected, however, that even more accurate and stable numerical results could be obtained by discretizing and integrating eqn (13) or eqn (14), together with eqn (9). Second-order terms $\mathrm{d}^2\gamma/\mathrm{d}t^2$ in eqn (15) are also calculated by backward finite time difference of earlier calculated $\mathrm{d}\gamma/\mathrm{d}t$ values.

The time step Δt is either fixed or adaptively calculated as a function of a constant mesh Courant number ($\simeq 0{\cdot}30$), based on maximum tangential velocity and minimum distance between nodes on the interface (see application in Section 4.2).

3.2 Spatial discretization

Using a boundary element method[18] (BEM), the VSs' boundary Γ is divided into M elements over which geometry $\mathbf{x}$ and vorticity γ are discretized using a set of m locally continuous polynomial shape functions $N_j(\mu)$, analytically defined on a reference element, with intrinsic coordinate μ varying between -1 and 1, using m discretization points (nodes). Hence, over element k,

$$x^k(\mu)=\sum_{j=1}^{m}N_j(\mu)x_j^k;\quad y^k(\mu)=\sum_{j=1}^{m}N_j(\mu)y_j^k;$$
$$\gamma^k(\mu)=\sum_{j=1}^{m}N_j(\mu)\gamma_j^k \tag{16}$$

where x_j^k, y_j^k, and γ_j^k denote nodal coordinates and vorticity for element k. Derivatives with respect to μ (μ-indices) are easily obtained from eqn (16), using explicit derivatives of shape functions.

Expressing BS eqn (4) in this discretization, we get, for nodal points $i=1,\cdots,N$, of coordinates (x_i, y_i) on the VSs,

$$u(x_i, y_i)=\frac{1}{2\pi}\sum_{k=1}^{M}\mathcal{P}\int_{-1}^{+1}\frac{y_i-y'^k(\mu)}{r_i^2(\mu)}\gamma'^k(\mu)s_\mu^k(\mu)\mathrm{d}\mu$$
$$v(x_i, y_i)=-\frac{1}{2\pi}\sum_{k=1}^{M}\mathcal{P}\int_{-1}^{+1}\frac{x_i-x'^k(\mu)}{r_i^2(\mu)}\gamma'^k(\mu)s_\mu^k(\mu)\mathrm{d}\mu \tag{17}$$

with $r_i=\{(x_i-x'^k(\mu))^2+(y_i-y'^k(\mu))^2\}^{1/2}$, and s_μ^k is the Jacobian of the transformation from element k to the reference element.

For BS eqn (8), we similarly get

$$u(x_i, y_i)=\frac{1}{2\lambda}\sum_{k=1}^{M}\mathcal{P}\int_{-1}^{+1}\times\frac{\gamma'^k(\mu)\sinh\frac{2\pi}{\lambda}(y_i-y'^k(\mu))}{\cosh\frac{2\pi}{\lambda}(y_i-y'^k(\mu))-\cos\frac{2\pi}{\lambda}(x_i-x'^k(\mu))}s_\mu^k(\mu)\mathrm{d}\mu$$
$$v(x_i, y_i)=-\frac{1}{2\lambda}\sum_{k=1}^{M}\mathcal{P}\int_{-1}^{+1}\times\frac{\gamma'^k(\mu)\sin\frac{2\pi}{\lambda}(x_i-x'^k(\mu))}{\cosh\frac{2\pi}{\lambda}(y_i-y'^k(\mu))-\cos\frac{2\pi}{\lambda}(x_i-x'^k(\mu))}s_\mu^k(\mu)\mathrm{d}\mu \tag{18}$$

In both eqns (17) and (18), dashed variables are calculated at μ, for each element k, using discretization (eqn (16)). Integrals in eqn (18) will be calculated by numerical integration (see next section).

To provide sufficient local continuity of both the discretized geometry and vorticity, the BEM discretization is based on using the middle interval of a 4-node cubic isoparametric element to interpolate between successive pairs of nodes on the boundary. In this method, developed by Grilli & Subramanya,[15] shape functions and interpolations of geometry and vorticity in eqn (16) are thus calculated within the cubic element, i.e. using 4 nodes, but only the middle interval is used, and remapped onto the

interval $[-1, +1]$, before integrations are performed. To interpolate between the next pair of nodes on the boundary, the element is slid forward by one node, and so forth.

Various components of evolution eqn (9) (with eqn (11)), are functions of 1st, 2nd and 3rd tangential s-derivatives along the boundary. Over each element k, these are expressed as $\partial/\partial s = (1/s_\mu^k)\partial/\partial\mu$ with, using eqn (12),

$$\cos\beta = \frac{x_\mu^k}{s_\mu^k};\ \sin\beta = \frac{y_\mu^k}{s_\mu^k};\ s_\mu^k = \{(x_\mu^k)^2 + (y_\mu^k)^2\}^{1/2} \tag{19}$$

and

$$\frac{\partial^2\beta}{\partial s^2} = \frac{y_{\mu\mu\mu}^k \cos\beta - x_{\mu\mu\mu}^k \sin\beta}{(s_\mu^k)^3} - \frac{3}{2(s_\mu^k)^4} \times [2x_{\mu\mu}^k y_{\mu\mu}^k \cos 2\beta - ((x_{\mu\mu}^k)^2 - (y_{\mu\mu}^k)^2)\sin 2\beta] \tag{20}$$

all of which could easily be calculated over each boundary element, using μ-derivatives of eqn (16). To calculate these s-derivatives and provide sufficient accuracy, however, particularly for the curvature, a 4th-order 5-node sliding isoparametric element[15] was first used. When this method was applied to highly distorted interfaces, however, computations rapidly failed after showing the initial trend of so-called VS roll-up,[10,8] and led to irregular motion of nodes, independently of flow conditions and physical properties. A repetition of these calculations using cubic splines to calculate the s-derivatives did not improve the results. A more detailed analysis of these problems[10] showed that the irregular motion of nodes was first triggered by inaccuracies in the higher-order s-derivatives, mostly at locations where a fairly non-uniform distribution of nodes occurred on the boundary. It was found that the mapping of geometric elements, with irregular node spacing, onto a reference element with constant node spacing created small errors in the high-order s-derivatives which, through time updating and enhanced surface tension effects (for instance in VS roll-up regions of high curvature; Fig. 1), rapidly propagated and led to sawtooth instabilities of the interface geometry.

A new method, referred to as parity mapping, was thus proposed by Hu and Grilli[10] to calculate s-derivatives more accurately. In this method, a monotonic mapping variable χ is defined, in between the transformation from s to μ, to create an element with node density similar to the geometric element. The parity element is then mapped onto a reference element with intrinsic coordinate μ varying between $[-1, +1]$ and irregular node spacing. Results showed that this method eliminates (or at least greatly reduces) fluctuations induced in tangential derivatives due to irregular node spacing. We believe that some of the problems pointed out in earlier studies,[6,11,3,13] and usually attributed to round-off and other errors in the integration of BS equations, might have been due to, or at least enhanced by, similar inaccuracies in the calculation of tangential derivatives.

Finally, when intense roll-up occurs, the VS's length may significantly increase. In order to maintain sufficient resolution of the discretization, the regridding method developed by Grilli & Subramanya[15] may be used to adaptively add and redistribute discretization nodes along the VSs (see the third application in this paper, and Hu & Grilli,[10] for applications of this method to VS roll-up).

3.3 Numerical integrations

At any given time t, the discretized BS eqn (17) or eqn (18) are numerically integrated to calculate velocities at N points i along the VSs. When point i does not belong to element k, integrals are regular and a simple Gauss quadrature rule is used. When point i belongs to element k, as indicated by eqn (3), since both z (i.e., z_i) and z' belong to boundary Γ, when $z' \to z$, a $1/|z - z'| \equiv 1/r_i$ hypersingularity occurs. In eqn (7) for the periodic cases, noting that[19]

$$\lim_{z'\to z} \cot\frac{\pi}{\lambda}(z - z') = \lim_{z'\to z} \times \left\{\frac{\lambda}{\pi(z - z')} - \frac{\pi}{3\lambda}(z - z') - O[(z - z')^3]\right\} = \frac{\lambda}{\pi}\lim_{z'\to z}\frac{1}{z - z'} \tag{21}$$

we expectedly get the same order hypersingularity.

The hypersingularity in BS equations will be analyzed using two methods: (i) the singularity will be removed from the integrals and evaluated using a direct Taylor series expansion of $(z - z')$ around the singular point, in a way similar to the method used by Cooker[20] for the complex potential (using the Cauchy integral theorem) and by Baker[21] for BS eqations (also used by Stansby & Slaouti[17] for periodic BS eqations); (ii) following the more general method proposed by Guiggiani *et al.*,[16] the singularity will be removed from the part of the integral performed over the reference element containing the singularity, using a Laurent series expansion in terms of polar coordinates centered on the singular point; a Taylor series expansion of $(\mathbf{x} - \mathbf{x}')$ will be expressed around the singular point to evaluate the terms in the series; final results will be shown to be identical to method (i).

3.3.1 Direct Taylor series expansion

In the neighborhood of the singular point we have $|z' - z|$ and $|s' - s| \ll 1$; hence, a truncated Taylor series expansion can be expressed as,

$$z' - z = (s' - s)z_s + \tfrac{1}{2}(s' - s)^2 z_{ss} + O[(s' - s)^3] \tag{22}$$

where subscripts denote partial differentiation. Therefore

$$\frac{1}{z' - z} = \frac{1}{(s' - s)z_s} - \frac{z_{ss}}{2z_s^2} + O[(s' - s)] \tag{23}$$

In view of eqn (23), the hypersingularity in BS eqn (3) (or eqn (7)) can be extracted as

$$q^*(z) = \frac{i}{2\pi}\int_{\Gamma(z')}\left\{\frac{\gamma(s')}{z-z'} - \frac{\gamma(s)}{(s-s')z_s}\right\}\mathrm{d}s' + \frac{i}{2\pi}\frac{\gamma(s)}{z_s}\int_{\Gamma(s')}\frac{\mathrm{d}s'}{s-s'} \tag{24}$$

The first integral is bounded for $z' \to z$ and can thus be accurately calculated by numerical integration. For a closed or a periodic boundary, the kernel of the last integral is a total differential, $-\mathrm{d}\ln|s-s'|$, which provides zero contribution to q^*.

For an arbitrary boundary, the singular part can be explicitly expressed by replacing eqn (23) into eqn (24), only for a small boundary segment Γ_s, of arclength Δs, symmetrically located around the singular point $z(s)$. We get

$$q^*(z) \simeq \frac{i}{2\pi}\int_{\Gamma(z')-\Gamma_s}\frac{\gamma(s')}{z-z'}\mathrm{d}s' + \frac{i}{2\pi}\int_{\Gamma_s}\left\{\frac{\gamma(s')-\gamma(s)}{z-z'} + \gamma(s)\frac{z_{ss}}{2z_s^2}\right\}\mathrm{d}s' + \frac{i}{2\pi}\frac{\gamma(s)}{z_s}\int_{s-\Delta s/2}^{s+\Delta s/2}\frac{\mathrm{d}s'}{s-s'} \tag{25}$$

In the second integral, according to eqn (22), the denominator of the first term can be approximated by $(s-s')z_s$; hence, the first term can be approximated by, $-\gamma_s/z_s$; the third integral, again, provides zero contribution. Multiplying up and down in the second integral by the complex conjugate z_s^*, we get

$$q^*(z) \simeq \frac{i}{2\pi}\int_{\Gamma(z')-\Gamma_s}\frac{\gamma(s')}{z-z'}\mathrm{d}s' + \frac{i}{2\pi z_s z_s^*}\Delta s\left\{-\gamma_s z_s^* + \gamma\frac{z_{ss}z_s^*}{2z_s}\right\}_{z(s)} \tag{26}$$

where the second term is evaluated at point $z(s)$. Finally, noting that $z_s z_s^* = 1$ and $z_{ss}z_s^* = -z_s z_{ss}^*$, we get

$$q^*(z) = u(s) - iv(s) \simeq \frac{i}{2\pi}\int_{\Gamma(z')-\Gamma_s}\frac{\gamma(s')}{z-z'}\mathrm{d}s' - \frac{i}{2\pi}\Delta s\left\{\gamma_s z_s^* + \gamma\frac{z_{ss}^*}{2}\right\}_{z(s)} \tag{27}$$

in which the integral can be calculated numerically and the second term can be written as $(u_0 - iv_0)$, with

$$u_0\big(x(s),\ y(s)\big) = -\frac{\Delta s}{2\pi}\left\{\gamma_s y_s + \frac{\gamma}{2}y_{ss}\right\}_{\mathbf{x}(s)}$$

$$v_0\big(x(s),\ y(s)\big) = \frac{\Delta s}{2\pi}\left\{\gamma_s x_s + \frac{\gamma}{2}x_{ss}\right\}_{\mathbf{x}(s)} \tag{28}$$

where all values are calculated at point $\mathbf{x}(s) = (x(s),\ y(s))$.

3.3.2 Laurent series expansion in the singular reference element

In discretized form, the integrand of BS eqn (17) or eqn (18) can be expressed as

$$F^{u,\ v}(\mu) = N_j(\mu)s_\mu^k(\mu)f_i^{u,\ v}(\mu) \tag{29}$$

where $f_i^{u,\ v}$ denotes one or the other kernels of the BS integrals. Since, as discussed above, both the non-periodic and the periodic BS equations show the same singular behavior near the singular point, for simplicity we will only consider the kernels of eqn (17).

Following Guiggiani *et al.*,[16] for each element k, the singularity in the integrand can be represented in the neighborhood of the singular point $\mathbf{x}_i$, of intrinsic coordinate μ_i on the reference element, by means of a Laurent series expansion of the form (Fig. 2)

$$F(\rho,\ \theta) = \frac{F_{-1}(\theta)}{\rho} + F_0(\theta) + O(\rho) \tag{30}$$

where $(\rho,\ \theta)$ denote polar coordinates centered on point μ_i in the reference element, and $F_0(\theta)$ and $F_{-1}(\theta)$ are $O(1)$ functions of the VS geometry around point i. The contributions of element k to the integrals in eqn (17) can thus be expressed as

$$I^k = \int_{-1}^{\mu_\ell} F(\rho(\mu),\ \theta(\mu))\mathrm{d}\mu + \int_{\mu_\ell}^{\mu_r}\left[\frac{F_{-1}(\theta)}{\rho} + F_0(\theta)\right]\mathrm{d}\mu + \int_{\mu_r}^{+1} F(\rho(\mu),\ \theta(\mu))\mathrm{d}\mu = I_1^k + I_2^k + I_3^k \tag{31}$$

where $(\mu_\ell,\ \mu_r)$ denotes a small interval containing the singular point μ_i.

The first and last integrals in eqn (31) are regular and can be calculated using the Gauss quadrature rule, after transformation of their respective intervals to $[-1, +1]$. The middle integral, I_2^k, is singular and can itself be divided into three parts, by defining a semicircular boundary of vanishing radius ϵ centered on the singular point, as

$$\begin{aligned} I_2^k = \lim_{\epsilon\to 0}\Bigg\{ &-\int_{\mu_i-\mu_\ell}^{\epsilon}\left[\frac{F_{-1}(\pi)}{\rho} + F_0(\pi)\right]\mathrm{d}\rho \\ &-\int_{\pi}^{0}\left[\frac{F_{-1}(\theta)}{\epsilon} + F_0(\theta)\right]\epsilon\sin\theta\,\mathrm{d}\theta \\ &+\int_{\epsilon}^{-\mu_i+\mu_r}\left[\frac{F_{-1}(0)}{\rho} + F_0(0)\right]\mathrm{d}\rho\Bigg\} \\ = F_{-1}(0)\ln\frac{\mu_r-\mu_i}{\mu_i-\mu_\ell} &+ \int_0^{\pi}F_{-1}(\theta)\sin\theta\,\mathrm{d}\theta \\ &+(\mu_i-\mu_\ell)F_0(\pi) + (\mu_r-\mu_i)F_0(0) \end{aligned} \tag{32}$$

where, by definition of the geometry on the intrinsic element, $\mu = \mu_i + \rho\cos\theta$ and the property $F_{-1}(\theta) = -F_{-1}(\theta+\pi)$ (which is a consequence of the residue theorem) have been used to combine the first (singular) terms in the first and last integrals.[16] If μ_ℓ and μ_r are selected symmetrically around point i, we have $\mu_i - \mu_\ell = \mu_r - \mu_i = \Delta\mu/2$, with $\Delta\mu = \mu_r - \mu_\ell$, and eqn (32)

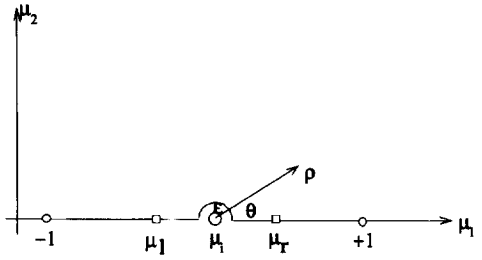

Fig. 2. Sketch relating to the singular integration at point i of reference element k.

further simplifies to

$$I_2^k = \int_0^{\pi} F_{-1}(\theta)\sin\theta d\theta + \frac{\Delta\mu}{2}[F_0(\pi)+F_0(0)] \tag{33}$$

Following the general method proposed by Guiggiani *et al.*,[16] the calculation of $F_0(\theta)$ and $F_{-1}(\theta)$ in eqn (33) first requires defining a local intrinsic coordinate expansion for the vector $\mathbf{x}-\mathbf{x}_i$ in the neighborhood of the singular point $\mathbf{x}_i$ (i.e., for small ρ), where $\mathbf{x}$ denotes another point of element k. To be able to account for changes or gradients perpendicular to the element in this expansion, a new coordinate system (μ_1, μ_2) is introduced, as indicated in Fig. 2, with the following relationships,

$$\mu_1 \equiv \mu = \mu_i + \rho\cos\theta \quad \text{and} \quad \mu_2 = \rho\sin\theta \tag{34}$$

as a function of the polar coordinate system introduced above; in this coordinate system, the singular point is defined as $(\mu_i, 0)$. We thus get

$$\begin{aligned}\mathbf{x}-\mathbf{x}_i = &\left.\frac{\partial\mathbf{x}}{\partial\mu_1}\right\}_{(\mu_i,\,0)}(\mu_1-\mu_i)+\left.\frac{\partial\mathbf{x}}{\partial\mu_2}\right\}_{(\mu_i,\,0)}\mu_2\\ &+\left.\frac{\partial^2\mathbf{x}}{\partial\mu_1\partial\mu_2}\right\}_{(\mu_i,\,0)}(\mu_1-\mu_i)\mu_2\\ &+\left.\frac{\partial^2\mathbf{x}}{\partial\mu_1^2}\right\}_{(\mu_i,\,0)}\frac{(\mu_1-\mu_i)^2}{2}+\left.\frac{\partial^2\mathbf{x}}{\partial\mu_2^2}\right\}_{(\mu_i,\,0)}\frac{\mu_2^2}{2}+\cdots\end{aligned} \tag{35}$$

Now, using the definitions of eqn (34), we have

$$\frac{\partial}{\partial\mu_2} = -\tan\theta\,\frac{\partial}{\partial\mu_1} \tag{36}$$

$$\frac{\partial^2}{\partial\mu_2^2} = \frac{\tan\theta}{\rho\sin\theta\cos\theta}\left(\frac{\partial\rho}{\partial\mu_1}-\frac{1}{\cos\theta}\right)\frac{\partial}{\partial\mu_1}+\tan^2\theta\frac{\partial^2}{\partial\mu_1^2}$$

and, combining eqn (35) with eqns (34) and (36), we get

$$\mathbf{x}(\mu)-\mathbf{x}_i = \rho(\mu)\mathbf{A}(\theta)+\rho^2(\mu)\mathbf{B}(\theta)+O(\rho^3) \tag{37}$$

with

$$\mathbf{A}(\theta) = \frac{d\mathbf{x}}{d\mu}(\mu_i)C(\theta)$$

$$\text{with}\quad C(\theta) = \cos\theta-\tan\theta\sin\theta+\frac{\tan^2\theta}{2}\left[\frac{d\rho}{d\mu}-\frac{1}{\cos\theta}\right] \tag{38}$$

and

$$\mathbf{B}(\theta) = \frac{d^2\mathbf{x}}{d\mu^2}(\mu_i)\left[\frac{\cos^2\theta}{2}+\sin^2\theta\left(\frac{\tan^2\theta}{2}-1\right)\right] \tag{39}$$

where the first and second components of $\mathbf{A}(\theta)=(A_1, A_2)$ and $\mathbf{B}(\theta)=(B_1, B_2)$ refer to the x and y coordinates, respectively.

Using eqns (37)–(39), we can now express various parts of $F(\mu)$ for BS eqn (17) and put them in the form of expansion (eqn (30)). After some calculations, we get

$$f_i^{u,\,v}(\rho(\mu),\,\theta(\mu)) = \frac{S_{-1}^{u,\,v}(\theta)}{\rho}+S_0^{u,\,v}(\theta)+O(\rho) \tag{40}$$

with

$$\begin{aligned}S_{-1}^{u,\,v}(\theta) &= \mp\frac{A_{2,\,1}(\theta)}{2\pi(A_1^2(\theta)+A_2^2(\theta))}\\ S_0^{u,\,v}(\theta) &= \mp\frac{B_{2,\,1}(\theta)-D(\theta)A_{2,\,1}(\theta)}{2\pi(A_1^2(\theta)+A_2^2(\theta))}\end{aligned} \tag{41}$$

and

$$D(\theta) = 2\frac{A_1(\theta)B_1(\theta)+A_2(\theta)B_2(\theta)}{A_1(\theta)^2+A_2(\theta)^2} \tag{42}$$

We also have

$$N_j(\rho(\mu),\,\theta(\mu))s_\mu^k(\rho(\mu),\,\theta(\mu)) = a_0(\theta)+a_1(\theta)\rho+O(\rho^2) \tag{43}$$

with

$$\begin{aligned}a_0 &= s_\mu^k(\mu_i)N_j(\mu_i)\\ a_1(\theta) &= C(\theta)[s_\mu^k(\mu_i)N_{\mu j}(\mu_i)+s_{\mu\mu}^k(\mu_i)N_j(\mu_i)]\end{aligned} \tag{44}$$

where μ-indices indicate derivatives. Hence, from eqn (30), we have

$$F_0^{u,\,v}(\theta) = a_0S_0^{u,\,v}(\theta)+a_1(\theta)S_{-1}^{u,\,v}(\theta);\quad F_{-1}^{u,\,v}(\theta) = a_0S_{-1}^{u,\,v}(\theta) \tag{45}$$

which gives the terms of the Laurent series expansion.

Using eqn (45), with eqns (41) and (44), one can now analytically calculate the integral in eqn (33) and show that it vanishes. Accounting for relationships between odd and even functions of θ at 0 and π, the second term in eqn (33) can also be calculated, using eqns (38)–(45), as

$$\frac{\Delta\mu}{2}[F_0^{u,\,v}(\pi)+F_0^{u,\,v}(0)] = \Delta\mu[a_0S_0^{u,\,v}(0)+a_1(0)S_{-1}^{u,\,v}(0)] \tag{46}$$

with $\mathbf{A}(0)=\mathbf{x}_\mu$, $\mathbf{B}(0)=\mathbf{x}_{\mu\mu}/2$, $C(0)=1$, and

$$D(0) = \frac{x_\mu x_{\mu\mu}+y_\mu y_{\mu\mu}}{(s_\mu^k)^2} \tag{47}$$

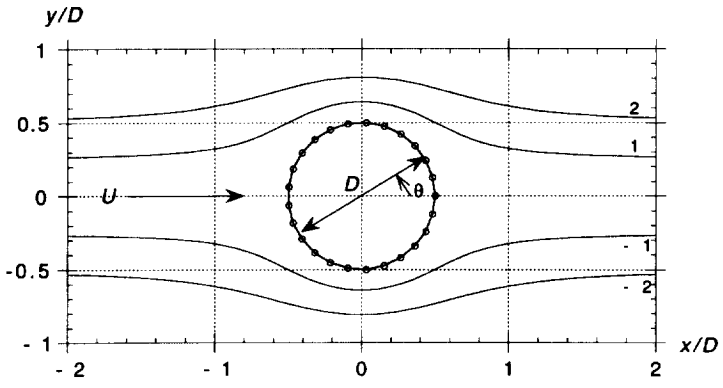

Fig. 3. Sketch of uniform flow of velocity U past a circular cylinder of diameter D. Numbers on streamlines correspond to constant values of the streamfunction ψ. (○) denote the N BEM discretization nodes on the VS/cylinder interface.

and hence

$$S_0^{u,\,v}(0) = \mp \frac{(y,\,x)_{\mu\mu}(s_\mu^k)^2 - 2(y,\,x)_\mu(x_\mu x_{\mu\mu} + y_\mu y_{\mu\mu})}{4\pi(s_\mu^k)^4}$$

$$S_{-1}^{u,\,v}(0) = \mp \frac{(y,\,x)_\mu}{2\pi(s_\mu^k)^2} \tag{48}$$

Using eqns (33) and (46), together with eqn (48), one can then, after some final transformations, calculate the singular part of eqn (31) as

$$I_2^k = \frac{\mp\,\Delta\mu}{2\pi s_\mu^k(\mu_i)}\left[N_{\mu_j}(y,\,x)_\mu + \tfrac{1}{2}N_j(y,\,x)_{\mu\mu}\right]_{\mu=\mu_i} \tag{49}$$

for the element k containing the singular point, i, in the first and the second BS integrals (17) or (18), respectively. All terms in eqn (49) can be expressed as a function of element shape functions and nodal values, using eqns (16) and (19).

3.3.3 Discussion

We will now show that eqn (49) is identical to eqn (28), derived using the first method. To do so, due to the BEM discretization, we first have to multiply eqn (49) by γ_j^k, the nodal vorticity for element k, and perform a summation over m nodes. We then need to replace $\Delta\mu = \Delta s/s_\mu^k$, $(y,\,x)_\mu = (y,\,x)_s s_\mu^k$ and $(y,\,x)_{\mu\mu} = (y,\,x)_{ss}(s_\mu^k)^2$ in the equation. We thus get, for the hypersingular contributions to BS equations,

$$(u_0,\,v_0)_i = \mp \frac{\Delta s}{2\pi}\left[\gamma_s(y,\,x)_s + \tfrac{1}{2}\gamma(y,\,x)_{ss}\right]_i \tag{50}$$

which is indeed identical to eqn (28).

In eqn (28) or eqn (49), the first and second derivatives of geometry and vorticity with respect to s or μ are needed at the singular point in order to calculate the hypersingular contributions to BS equations. Hence, this justifies using both a higher-order discretization and accurate methods for calculating the s-derivatives in the numerical model.

Since our BEM model is based on using, and integrating within, a reference element, method (ii), leading to eqn (49), is the relevant one for the model. Furthermore, if needed, this method can more easily be extended to even higher-order representation of hypersingularities, by keeping more terms in the Laurent series (eqn (30)) and other related expansions.

4 APPLICATIONS

Validation tests are first conducted to evaluate the numerical accuracy of BS integrals for a steady uniform flow past a circular cylinder; results are compared with the analytical solution. The propagation of an exact nonlinear free surface periodic wave over constant depth (a so-called streamfunction wave (SFW)) is calculated next, also to test the time marching procedures. Finally, an application of the model to the periodic KH instability at the interface between two fluids is presented.

4.1 Steady flow past a circular cylinder

Fig. 3 shows the set-up for the computation of a uniform flow of velocity U past a circular cylinder of diameter D. In this simple case, the complex potential is found by superposing the potentials for a uniform flow and for a doublet, in which the strength is such as to get a separation streamline on the cylinder boundary.[1] We thus get

$$\Phi(z) = U\left(z + \frac{D^2}{4z}\right) \tag{51}$$

from which the potential and the streamfunction read

$$\phi(r,\,\theta) = U\sin\theta\left(r + \frac{D^2}{4r}\right)$$

$$\psi(r,\,\theta) = U\cos\theta\left(r - \frac{D^2}{4r}\right) \tag{52}$$

respectively, where $(r,\,\theta)$ denote polar coordinates centered on the cylinder (Fig. 3), and the water velocity components read

$$u_c(r,\,\theta) = U\left\{1 - \frac{D^2}{4}\frac{\cos 2\theta}{r^2}\right\}$$

$$v_c(r,\,\theta) = U\frac{D^2}{4}\frac{\sin 2\theta}{r^2} \tag{53}$$

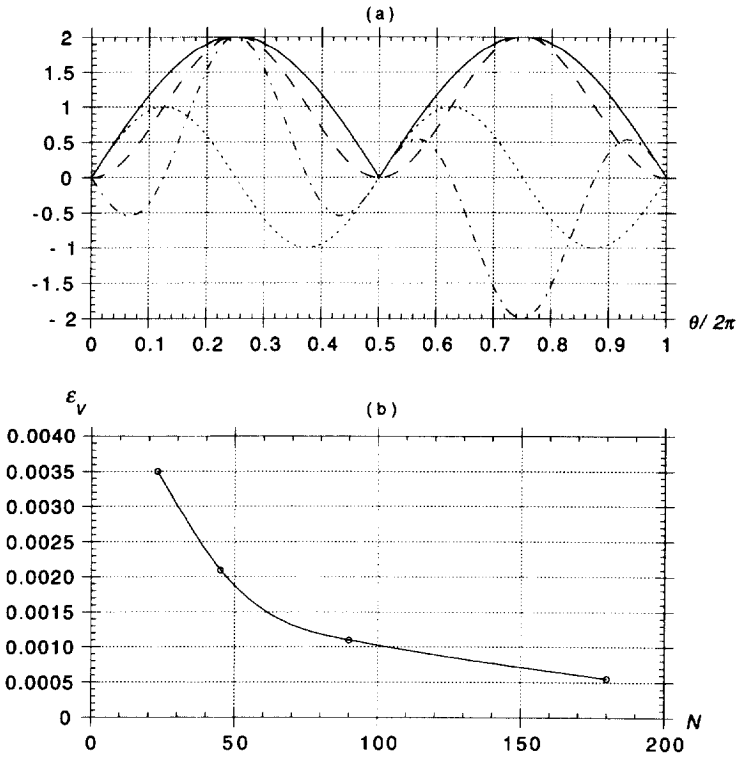

Fig. 4. Uniform flow of velocity U past a circular cylinder of diameter D. (a) Values on the cylinder of: (— —) u_c/U; (- - - -) v_c/U; (- - -) γ/U; and (—) $V_c = \sqrt{u_{c^2} + v_{c^2}}$, as a function of the angular position $\theta/2\pi$ (see Fig. 3). (b) Numerical error (○), $\varepsilon_V = \max|(V_{BEM} - V_c)/V_{BEM}|$, as a function of the number of BEM nodes N; (—) least-square fit to the results, $\varepsilon_V \propto N^{-1}$.

respectively, with the total velocity $V_c = |\mathbf{u}_c| = \sqrt{u_c^2 + v_c^2}$. According to the definition of VSs, the circulation on the cylinder is ($r = D/2$)

$$\gamma(\theta) = \Delta V_s = V_{cs} = \mathbf{u}_c \cdot \mathbf{s} = u_c(D/2,\ \theta)\sin\theta - v_c(D/2,\ \theta)\cos\theta \qquad (54)$$

in which $\mathbf{s}$ denotes the tangential vector to the cylinder and V_{cs} is the water tangential velocity. In Fig. 3, a few streamlines corresponding to $\psi = \pm 1$ and ± 2 have been plotted according to eqn (52) and, in Fig. 4(a), the velocity components, total velocity and circulation have been plotted around the cylinder boundary using eqn (53) for $r = D/2$, and eqn (54).

In this application, the velocity components (u, v) and total velocity V on the VS/cylinder boundary are computed, in various BEM discretizations, using BS eqn (17). For simplicity, we use $U = D = 1$ and the exact circulation γ from eqn (54) is specified as input to the model. According to the definition, the total flow velocity is calculated as $V_{BEM} = 2V$, and the maximum error between the computed and analytical flow velocities, $\varepsilon_V = \max|(V_{BEM} - V_c)/V_{BEM}|$, is calculated and plotted in Fig. 4 as a function of the number of nodes in the discretization, N = 23, 45, 90 and 180. We see on the figure that ε_V is cut by roughly half each time the number of nodes is doubled. (In fact, a least-square fit to the results gives, $\varepsilon_V \propto N^{-1}$.) As both u and v, as well as the geometry, vary fairly smoothly around the cylinder, a small number of nodes with cubic interpolation in between is sufficient to well represent their variation; hence, the observed error behavior reflects that, in this case, the accuracy of the integrations is not too dependent on the interpolation of fields and is just proportional to the number of elements, i.e. integration points, used.

These results confirm both the accuracy and the convergence of the numerical integration methods used for calculating regular and singular terms in BS equations.

4.2 Propagation of a periodic surface wave

Finite amplitude periodic surface waves over constant depth h_0 can be generated with the accurate numerical method developed by Dalrymple;[22] this method applies Dean's streamfunction wave theory in a coordinate system moving with the wave celerity $c = \lambda/T$ (with λ the wavelength and T the wave period). The streamfunction wave solution is defined as

$$\psi(\theta,\ y) = \sum_{j=1}^{J} X(j)\sinh jk(h_0 + y)\cos j\theta - (U - c)y \qquad (55)$$

with $\theta = k(x - ct)$, the phase, and $X(j)$ a set of J coefficients, which are numerically calculated for the solution (eqn (55)) to satisfy the kinematic and dynamic boundary conditions on the free surface Γ_f, a no flow condition on the bottom Γ_b, and specified wave height and wavelength (H, λ) (Fig. 5). As part of Dalrymple's solution, the shape of the wave

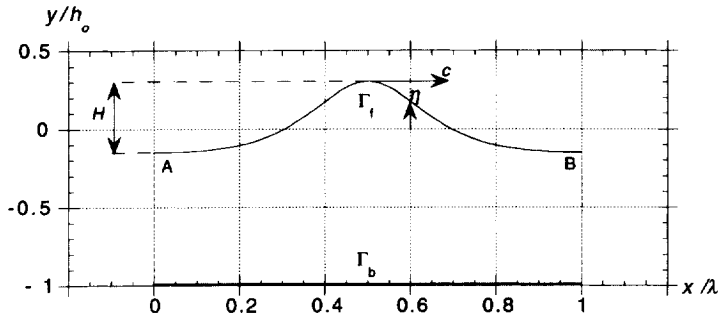

Fig. 5. Sketch of a finite amplitude streamfunction wave of height H and length λ propagating over constant depth h_0.

is also found, as η_j, at a set of J points on the free surface with phase $\theta_j = (j-1)\pi/(J-1)$. (Note that the wave height is defined as the distance from crest to trough, i.e. $H = \eta(0{\cdot}5) - \eta(0)$ in Fig. 5.) Wave particle velocity components (u_w, v_w) are obtained from eqn (55) as

$$u_w(\theta, y) = -\frac{\partial \psi}{\partial y}$$

$$= -\sum_{j=1}^{J} (jk)X(j)\cosh jk(h_0 + y)\cos j\theta + (U - c)$$

$$v_w(\theta, y) = \frac{\partial \psi}{\partial x} = -\sum_{j=1}^{J} (jk)X(j)\sinh jk(h_0 + y)\sin j\theta \tag{56}$$

In this application, the periodic BS eqn (18) and the time marching algorithm (eqn (15)) are used to propagate a wave, defined as above, over a fixed number of periods, in a coordinate system moving with the wave (i.e. at velocity c). Two VSs are used, one on the free surface Γ_f and one on the bottom Γ_b (Fig. 5), and each is discretized with N nodes per wavelength λ. In this coordinate system, the wave should appear to be stationary. Since the VSs' velocity is half the water velocity, however, the nodes, which follow the VSs' motion, move slower than the wave and hence change their position along the VS interfaces — and thus their circulation — as a function of time. The regridding method applied at each time step ensures that the distribution of nodes stays constant along the wave. The BEM model is initialized, using velocities (eqn (56)) to calculate the vorticity γ on the free surface and on the bottom as

$$\gamma(\theta, y) = V_{ws} = u_w(\theta, y)\cos\beta + v_w(\theta, y)\sin\beta \tag{57}$$

for $y = \eta$ and $y = -h_0$, respectively, with $\cos\beta$ and $\sin\beta$ defined as in eqn (12). To initialize the time marching algorithm, $d\gamma/dt$ is similarly calculated using eqn (9), in which the VSs' tangential acceleration is calculated from eqn (11). In this equation, according to the definition, the VS's velocity and particle acceleration are given by

$$\mathbf{u} = \tfrac{1}{2}\mathbf{u}_w$$

$$\frac{d\mathbf{u}}{dt} = \tfrac{1}{2}\frac{\partial \mathbf{u}_w}{\partial t} + \tfrac{1}{4}\left\{u_w\frac{\partial \mathbf{u}_w}{\partial x} + v_w\frac{\partial \mathbf{u}_w}{\partial y}\right\} \tag{58}$$

Partial derivatives of wave velocity components with respect to (x, y, t) can be obtained from eqn (56). Periodicity conditions are specified at nodes A and B on the free surface (Fig. 5), and similarly on the bottom, to more accurately calculate the BS integrals, and various terms involving s-derivatives in the time marching algorithm. For the latter, in particular, up to three nodes are added at each extremity, beyond points A and B, with values taken one wavelength apart inside the domain.

In the numerical tests, a wave of height $H = 0.1$ m, period $T = 3.1416$ s and length $\lambda = 6.895$ m ($c = 2.195$ m s^{-1}) is generated in depth $h_0 = 0.5$ m by the method of Dalrymple,[22] and used to initialize the BEM model as described above. (This wave is a moderately steep intermediate water wave with $H/h_0 = 0.2$ and $H/L = 0.0145$.) To adjust to the BEM discretization, the VSs' velocities are first recalculated using BS equations. The wave is then propagated over four periods, successively using numbers of nodes $N = 41$, 61, 81 and 101, for both the free surface and the bottom discretizations. Nodes are initially located at equal arclength distance on the VSs and, during time stepping, regridding is applied to redistribute the nodes at equal distance. To analyze the accuracy of the time marching algorithm, the time step is set to three successive values, $\Delta t = T/500$, $T/1000$ and $T/2000$, and maintained constant throughout computations. Hence, 12 sets of computations with different spatio-temporal discretizations are made.

Fig. 6(a) shows the error on wave height H, $\varepsilon_H = (H_{BEM} - H)/H$, as a function of dimensionless time t/T, for $\Delta t = T/1000$ and for the four discretizations; ε_H gradually decreases as N increases. Using a similar wave propagation model based on potential flow theory, Grilli & Subramanya[15] found that, for a given spatial discretization, numerical errors were minimum when the mesh Courant number, $C_0 = \Delta t'/\Delta x' \simeq 0.35$, in which dashes indicate non-dimensional variables and Δx is the minimum distance between nodes in the discretization. In the present case, we have $\Delta x' = \Delta x/\lambda \simeq 1/(N-1)$, hence $C_0 \simeq \Delta t'(N-1)$, with $\Delta t' = \Delta t\sqrt{g/\lambda} = 0.0075$, 0.0037 and 0.0019 for the three different time steps, respectively. Fig. 6(b) and (c) show the RMS and maximum errors on wave elevation for the 12 test cases, $\varepsilon_\eta = (\max \text{ or RMS})_i|(\eta_{BEM_i} - \eta_i)/\eta_i|$, as a function of C_0. (Note that, for $N = 101$ and $\Delta t' = 0.0075$,

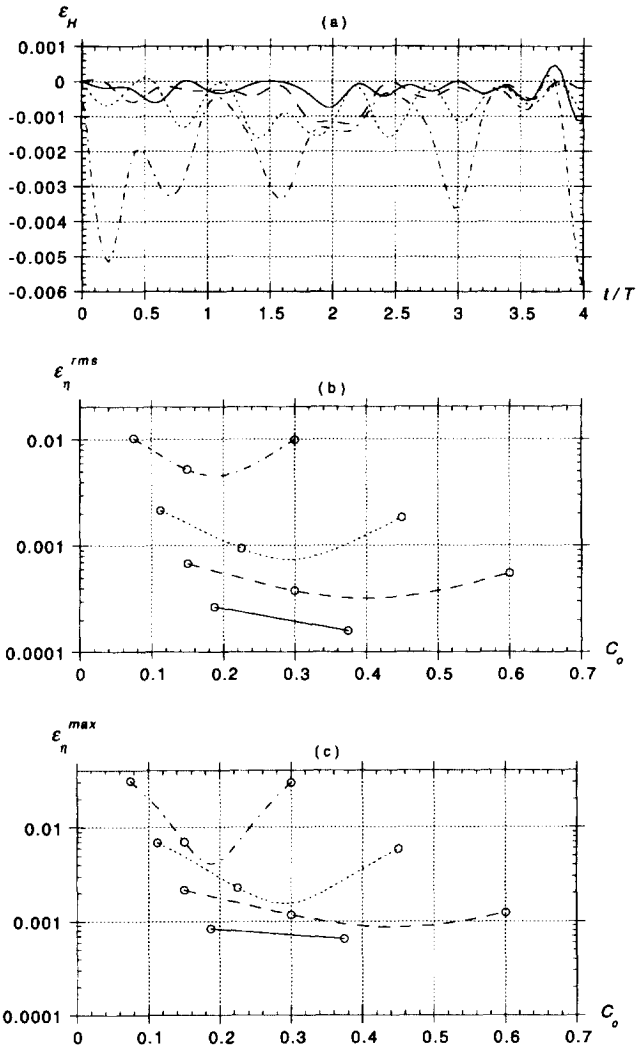

Fig. 6. Numerical errors for the propagation of a wave of height H and length λ in depth h_0 over four periods, with $N = (- - -)$ 41; $(- - - -)$ 61; $(- -)$ 81; and $(—)$ 101. The mesh Courant number is $C_0 \simeq \Delta t'(N-1)$, with, $\Delta t' = T'/500$, $T'/1000$ or $T'/2000$. (a) Errors on wave height, $\varepsilon_H = (H_{BEM} - H)/H$, for $\Delta t' = T'/1000$. (b) (○) Root mean square errors on wave elevation, $\varepsilon_\eta^{rms} = (RMS)_i|(\eta_{BEM_i} - \eta_i)/\eta_i|$. (c) (○) Maximum errors on wave elevation, $\varepsilon_\eta^{max} = (max)_i|(\eta_{BEM_i} - \eta_i)/\eta_i|$.

computations became unstable before the wave could propagate over four periods; hence, one result is missing in Fig. 6(b) and (c) for this combination of parameters.) Looking at the results, we see that there is indeed an optimum Courant number range, around $C_0 = 0.2$ to 0.4, for which both errors are minimum for each spatial discretization.

More specifically, for a given spatial discretization (i.e. N or Δx), decreasing the time step below the optimal C_0 does not lead to better results, unless Δx is similarly reduced (or N is increased), in order to stay within the optimal range of Courant number values. In this case, errors increase, probably due to increased round-off errors when many small time steps are used to propagate the wave. Similar observations can be made beyond the optimal C_0 range where, for a given spatial discretization, errors increase with C_0 (i.e. $\Delta t'$) at a fairly high rate; in fact, one could show that $\varepsilon_\eta \propto (\Delta t')^3$, corresponding to the truncation error of the Taylor series used in the time marching algorithm. These observations are consistent with the earlier results of Grilli & Subramanya.[15] Looking at points corresponding to the same time step on different curves in Fig. 6(b) and (c) (for instance, the smaller time step results with $\Delta t' = 0.0019 = T'/2000$ at the first (∘) on each curve), we see that, in accordance with the results in Fig. 6(a), errors keep decreasing at a high rate when C_0 (i.e. N) is increased. In fact, a least-square fit to each set of results in Fig. 6(b) or (c) for $\Delta t' = \text{cst}$ gives $\varepsilon_\eta \propto N^{-4}$.

Overall, Fig. 6(b) and (c) show that, in all cases, provided the Courant number is close to the optimal value, small errors (less than 0.5%) are obtained in the model after 2000 to 8000 time steps of wave propagation. Hence, this indicates the good accuracy of the time marching algorithm, combined with the accurate discretization and integration of the periodic BS equations, in the model.

4.3 Periodic KH instability

One case of periodic KH instability (Fig. 1) is now presented for a very unstable pure shear flow problem, with a velocity jump $\Delta U = U_0 - U_1 = 0.5\ \text{m s}^{-1}$ applied between two layers of an identical inviscid fluid with, hence, $\varphi = 1$ and $\kappa = \sigma_{01} = 0$. The initial amplitude of perturbation is $a = 0.0025$ m and the wavelength is selected as $\lambda = 0.1$ m, corresponding to an instability at the ripple scale (the wavelength, however, does not matter in this problem and results would be self-similar for another wavelength[10]). The initial vorticity $\gamma(\mathbf{x}, 0)$ on the interface is calculated assuming a linearized perturbation.[10]

The initial discretization has $N = 101$ equally spaced nodes per wavelength; more nodes are added through regridding at each time step, in order to maintain a constant spatial resolution as the VS length increases when the KH instability develops. To ensure high accuracy, the initial (non-dimensional) time step is set to a small value corresponding to a mesh Courant number $C_0 = 0.2$, i.e. at the lower bound of the optimal range (see previous section). We thus get $\Delta t' = \Delta t\sqrt{g/\lambda} = C_0/(N-1) = 0.002$, i.e. $\Delta t = 0.0002$. In the present application, however, a different non-dimensional time is used, based on the velocity jump at the interface, $\tau = t\Delta U/\lambda$; hence, the present non-dimensional time step is $\Delta\tau = \Delta t \Delta U/\lambda = 0.001$. Since the spatial resolution is maintained constant through regridding, the time step (and the mesh Courant number) also stay constant throughout computations. Periodic BS eqn (18) and the time marching algorithm (eqn (15)) are used to calculate the interfacial instability as a function of time. One wavelength is discretized and periodicity conditions are specified at each extremity. Model results for the time evolution of the interface over 3000 time steps are given in Fig. 7. At the end of computations, the

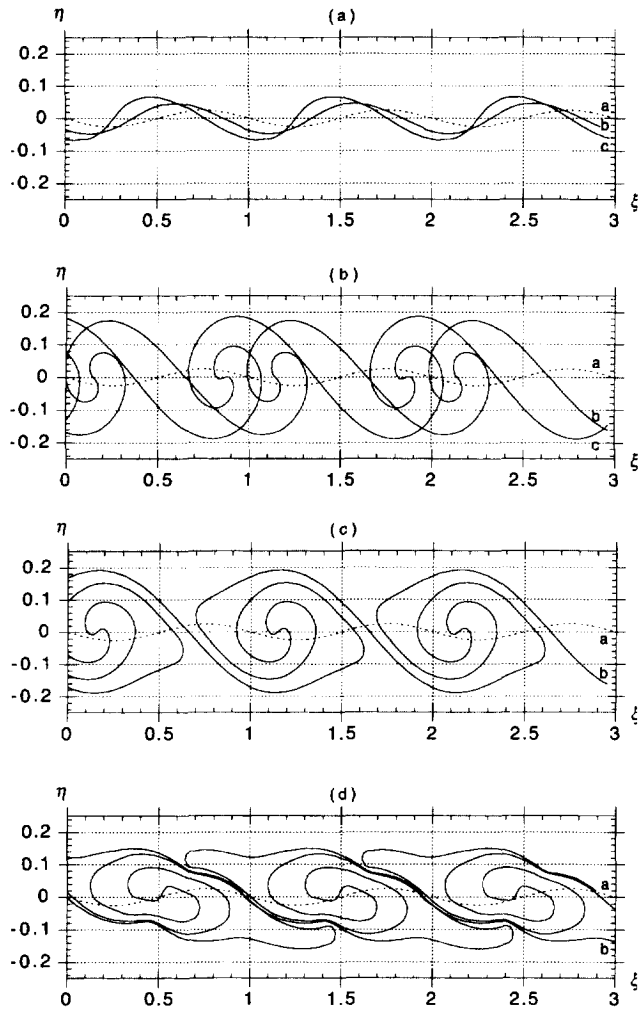

Fig. 7. Interface shape ($\xi = x/\lambda, \eta = y/\lambda$) for periodic KH instability with wavelength $\lambda = 0.1$ m, $\Delta U = 0.5$ m s^{-1}, $\varphi = 1$ and $\sigma_{01} = 0$, at non-dimensional time $\tau = t\Delta U/\lambda$ = (a) a: 0.001, b: 0.301, c: 0.601; (b) a: 0.001, b: 1.651, c: 1.951; (c) a: 0.001, b: 2.701; (d) a: 0.001, b: 3.001.

number of nodes has increased to $N = 328$ per wavelength (Fig. 7(d), curve b).

Overall, results show reasonable predictions of VS evolution. In Fig. 7(a), for small time, the interface perturbation slowly grows up while more or less preserving its initial shape; the initial growth rate in fact closely follows the linear growth rate[2,10] and, hence, this is referred to as the quasi-linear regime. At the same time, a relative motion of crests is observed; this phenomenon, which is not observed in point-vortex models,[8,4] indicates that, as the instability develops, interfacial waves travel at a modified phase velocity. In Fig. 7(b) it is seen that, after the quasi-linear initial growth, the larger nonlinearity in the flow field leads to both increased wave amplitude and skewness and, eventually, to a crest overturning similarly to a surface wave breaking; this is referred to as the nonlinear regime. In Fig. 7(c), the similarity of results with surface waves disappears as the interface VS rolls-up. In Fig. 7(d), as time further increases, the interface roll-up becomes more pronounced and, as the 'roll-up cells' become more elongated, the amplitude of disturbance starts gradually to decrease.

5 CONCLUSIONS

A higher-order boundary element model (BEM), based on hypersingular Biot–Savart equations, was proposed for the modeling of vortex sheets (VSs) representing interfaces between fluids moving at different velocities (shear layers). Depending on the case, periodic or non-periodic BS equations were used. An explicit Taylor expansion scheme, based on Lagrangian time derivatives with respect to the VSs' motion, was proposed for the updating of both the geometry and vorticity of the VSs, thus defining a time marching algorithm which allowed the modeling of VS dynamics.

In the BEM model, integrations were performed numerically on the reference element. Hypersingular terms in the integrals were explicitly expressed in two ways, using perturbation expansions around the singular points; both approaches were shown to give identical results, but the approach based on Giuggiani *et al.*'s[16] method is more general and, if needed, should be more easily extended to higher-order accuracy and/or degree of hypersingularity.

The integration of BS equations, using a cubic representation of both the geometry and the vorticity, was first tested for the steady-state case of a uniform flow past a circular cylinder. In this special example, convergence of the results toward the analytic solution, with the refinement of the discretization, was shown to be $\propto 1/N$, where N is the number of nodes. The propagation over constant depth of a permanent form, finite amplitude surface wave was tested next. A numerically exact solution[22] was used to initialize the BEM model, and errors on both wave height and wave shape were calculated for the propagation over four time periods (i.e. four wavelengths or 27.6 times the depth in the present case). For each spatial discretization, errors were shown to be minimum when the time step was such as to achieve a mesh Courant number $C_0 \simeq 0.30$; beyond the optimal C_0, errors increased with $(C_0)^3$, corresponding to the truncation error, $(\Delta t')^3$, of the time marching algorithm. This is similar to earlier results by Grilli & Subramanya.[15] In all cases, for a constant time step, errors decreased as $\propto 1/N^4$. Although the resolution of the wave discretization was maintained constant through regridding, an adaptive time stepping procedure could be used, as in Grilli & Subramanya,[15] to accommodate varying spacing between discretization nodes while achieving an optimal C_0 value.

In a final application, the Kelvin–Helmholtz (KH) instability of a pure shear flow between two layers of a fluid moving at different velocities was presented. The interface was initially sinusoidally perturbed and computations showed a rapid growth of instability, leading to intense

interface/VS roll-up. It is worth pointing out that standard point-vortex or PCVS computations usually fail before the stage of Fig. 7(b), whereas the present model provides very stable numerical results for the full stages of development of VS roll-up. More cases of KH instability calculated using this model, particularly for different fluids (i.e. oils with different density and oil/water interfacial tension), will be presented in a forthcoming paper, and results for the interfacial shape and growth rate will be analyzed in detail (Hu and Grilli[23]).

ACKNOWLEDGEMENTS

This research was supported by the United States Coast Guards (Oil Pollution Research Grant Program, District No. 1) and Minerals Management Services, through a grant of the US Department of Transportation, No. DTRS-5795-G-00065, FY 1995, 1996. The information reported in this work does not necessarily reflect the position of the US Government.

REFERENCES

1. Batchelor, G. K. *An Introduction to Fluid Dynamics*. Cambridge University Press, Cambridge, 1967.
2. Lamb, H. *Hydrodynamics*, 6th edition. Cambridge University Press, Cambridge, 1932.
3. Moore, D. W. A numerical study of the roll-up of a finite vortex sheet. *J. Fluid Mech.*, 1974, **63**(2), 225–235.
4. Rangel, R. H. and Sirignano, W. A. Nonlinear growth of Kelvin–Helmholtz instability: effect of surface tension and density ratio. *Phys. Fluids*, 1988, **31**(7), 1845–1855.
5. Zaroodny, S. J. and Greenberg, M. D. On a vortex sheet approach to the numerical calculation of water waves. *J. Comp. Phys.*, 1973, **11**, 440–446.
6. Fink, P. T. and Soh, W. K. A new approach to roll-up calculations of vortex sheets. *Proc. R. Soc. Lond.*, 1978, **A362**, 195.
7. Van de Vooren, A. I. A numerical investigation of the rolling up of vortex sheets. *Proc. R. Soc. Lond.*, 1980, **A373**, 67–91.
8. Grilli, S. T., Hu, Z. & Spaulding, M. L. Numerical modeling of oil containment by a boom. In *Proc. 19th Arctic and Marine Oil Spill Prog. Tech. Seminar*, AMOP, Vancouver, Canada, June 1996, pp. 343–376. Environment Canada, 1996.
9. Baker, G. R., Meiron, D. I. and Orszag, S. A. Generalized vortex method for free-surface flow problems. *J. Fluid Mech.*, 1982, **123**, 477–501.
10. Hu, Z. & Grilli, S. T. Computation of periodic instability of stratified fluid using continuous vortex sheet dynamics. In *Proc. 1997 ASME Fluid Eng. Div. Summer Meeting*, Vancouver, Canada, June 1997. Paper No. FEDSM97-3502.
11. Krasny, R. A study of singularity formation in a vortex sheet by the point-vortex approximation. *J. Fluid Mech.*, 1986, **167**, 65–93.
12. Jones, W. T. Instability at an interface between oil and flowing water. *J. Basic Eng.*, 1972, **94**, 874–878.
13. Moore, D. W. The spontaneous appearance of a singularity in the shape of an evolving vortex sheet. *Proc. R. Soc. Lond.*, 1979, **A365**, 105.
14. Meiron, D. I., Baker, G. R. and Orszag, S. A. Analytic structure of vortex sheet dynamics, Part 1. Kelvin–Helmholtz instability. *J. Fluid Mech.*, 1982, **114**, 283–298.
15. Grilli, S. T. and Subramanya, R. Numerical modeling of wave breaking induced by fixed or moving boundaries. *Comput. Mech.*, 1996, **17**(6), 374–391.
16. Guiggiani, M., Krishnasamy, G., Rudolphi, T. J. and Rizzo, F. J. A general algorithm for the numerical solution of hypersingular boundary integral equations. *Trans. ASME*, 1992, **59**, 604–614.
17. Stansby, P. K. and Slaouti, A. On nonlinear wave interaction with cylindrical bodies: a vortex sheet approach. *Appl. Ocean Res.*, 1984, **6**(2), 108–115.
18. Brebbia, C. A. *The Boundary Element Method for Engineers*. John Wiley & Sons, New York, 1978.
19. Abrahmowitz, M. & Stegun, I. *Handbook of Mathematical Functions*. Dover Publications, New York, 1972, pp. 360–361.
20. Cooker, M. J. A boundary-integral method for water wave motion over irregular bed. *Eng. Anal. Bound. Elem.*, 1990, **7**(4), 205–213.
21. Baker, G. R. A test of the method of Fink and Soh for following vortex-sheet motion. *J. Fluid Mech.*, 1980, **100**(1), 209–220.
22. Dalrymple, R. A. A finite amplitude wave on a linear shear current. *J. Geophys. Res.*, 1974, **78**(30), 4498–4504.
23. Hu, Z. & Grilli, S. T. Study of nonlinear Kelvin–Helmholtz instability including gravity, surface tension and interfacial friction effects (in preparation).